Depth-sensing thermal stability of accumulative fold-forged nanostructured materials

F. Khodabakhshi [a,*], A.P. Gerlich [b], D. Verma [c], M. Nosko [d], M. Haghshenas [e]

[a] School of Metallurgy and Materials Engineering, College of Engineering, University of Tehran, P.O. Box: 11155-4563, Tehran, Iran
[b] Department of Mechanical and Mechatronics Engineering, University of Waterloo, Waterloo, ON, Canada
[c] Nanoscience Instruments, 10008 S. 51st Street, Suite 110, Phoenix, AZ 85044, USA
[d] Institute of Materials and Machine Mechanics, Slovak Academy of Sciences, Dúbravská cesta 9/6319, 845 13 Bratislava, Slovak Republic
[e] Micro/Nano-Mechanics Laboratory, Department of Mechanical Engineering, University of Toledo, OH, USA

HIGHLIGHTS

- The UFG alloy and NS nanocomposite were produced by the new AFF route.
- Formation of nano-grains and nanoparticles dispersion studied.
- Depth-sensing thermal property interrogated the more stability of nanocomposite.
- The importance of nanoparticles is retarding the coalescence of nano-grains.

GRAPHICAL ABSTRACT
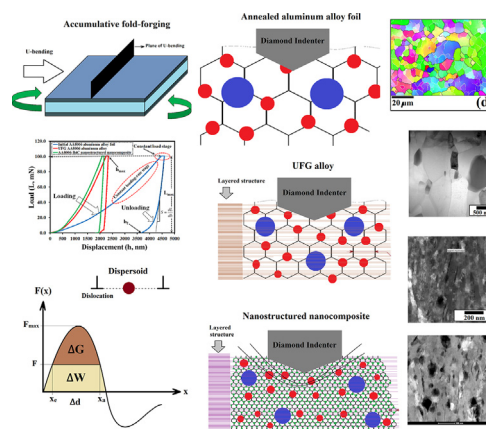
ARTICLE INFO

ABSTRACT

Accumulative fold-forging (AFF) as a newly developed severe plastic deformation (SPD) process based on the repetitive fold-forging steps is implemented for the production of the layered UFG (~200 nm) AA8006 alloy and AA8006-B₄C nanocomposite (~35 nm, 10 vol%) materials from the initial AA8006 alloy foil. The remarkably refined grains and nanoparticles can control metallic materials' mechanical properties, including the strength, strain rate dependency, and thermal stability behavior. In this context, nano-grains' local mechanical response during nanoindentation can vary considerably depending on the testing temperature, and this has yet to be discussed. In this research, after materials characterization of produced nanostructured materials according to the AFF route, the relating depth-sensing thermal stability of them assessed by conducting the nanoindentation testing at different temperatures in the range of 300–523 K. Depth sensing softening behavior is elaborated to identify the low-temperature thermal stability of processed materials. The results enunciated the occurrence of thermal softening by refining the grain structure. However, introducing the reinforcing nanoparticles lead to a pinning action that stabilized the grain boundaries.

1. Introduction

It is well-known that ultra-fine grained (UFG) and nanostructured (NS) metals and alloys, as well as metal-matrix nanocomposites, offer

* Corresponding author.
E-mail address: fkhodabakhshi@ut.ac.ir (F. Khodabakhshi).

exceptional strength to weight ratios along with other interesting functional properties such as fatigue strength and superplastic behavior, making them attractive candidates for practical applications in various automotive, aerospace, microelectronics, and biomedical industries [1–3]. Two possible approaches introduced for grain refinement to the ultra-fine and nanoscale; one is aided by rapid cooling during consolidation or solidification of material similar to melt spinning (MS) process [4,5], and the other based on the extensive accumulative straining in the form of severe plastic deformation (SPD) [6–8]. The production rate and size of components can restrict the first concept; nevertheless, the second approach has the potential for large-scale production in industrial applications [9,10]. Incidentally, several SPD methods were proposed and implemented for the production of UFG and nanostructured materials both in the bulk and sheet forms [11,12], such as; equal channel angular pressing (ECAP) [13,14], high-pressure torsion (HPT) [15,16], accumulative roll bonding (ARB) [17,18], constrained groove pressing (CGP) [19], cryogenic friction stir processing (CFSP) [20], and newly accumulative fold forging (AFF) [21–23]. It is worth noting that several of these SPD methods, including; ECAP, ARB, FSP, and AFF processes, can combine during UFG/NS formation to incorporate reinforcing nanoparticles into the structure to fabricate the ultra-fine grained or nanostructured metal-matrix nanocomposites [24,25].

As described before, imposing intense plastic strains into the material through SPD generates a massive number of statistical and geometrically necessary dislocations. Subsequently, these can rearrange via further straining to form arrays of sub-grains by transforming them into low- and high-angle grain boundaries [26–29]. One of the main drawbacks of interface-controlled UFG and NS alloy and nanocomposite materials processed through the SPD route would be enhanced elemental diffusion at elevated temperatures along the broad area of grain boundaries, leading to degraded thermal stability that can lead to accelerated creep phenomena such as grain boundary sliding [30–32]. The current research work's essential contribution focuses on pinning grain boundaries by introducing secondary phase reinforcing nanoparticles to restrict the grain boundary diffusion and sliding mechanisms to achieve higher service temperatures. The gift of strengthening nanoparticles to reduce the energy of generated grain boundaries following SPD may enhance elevated temperature due to semi-stabilized nanograins [33,34]. However, this is not well addressed in the literature.

Therefore, in the present research, UFG and NS materials' localized thermal stability processed according to the SPD concept was assessed. This work focuses on implementing the AFF process as an advanced SPD route because of its incredible capacity for creating a massive number of nano-sized layers through a small thickness of material after consolidation. The specific application for these layered alloy and composite materials treated by AFF processing route could be the damping tools for controlling the mechanical vibrations in electronic devices because of the excellent capacity caused by the contribution of a multi-million number of nano-layers and interfaces across the produced layered composite structure. These samples also have the excellent potential for implementing as the storage materials considering the large fraction of surface boundaries inside the structure. After processing nanostructural materials via the newly developed AFF technique, the focus was on further characterizing the AA8006-B$_4$C aluminum-matrix nanocomposite system. The microstructural features and characteristics of the accumulative fold-forged aluminum alloy and nanocomposite materials investigated by field emission-scanning electron microscopy (FE-SEM), standard and high-resolution transmission electron microscopy (TEM/HR-TEM), and electron backscattering diffraction (EBSD) analyses. Hot nanoindentation testing was then conducted on these processed materials in the temperature range of 300 to 523 K to elaborate on their thermal dependency and possible stabilities. The stiffness was quantified based on the shape and scale of loading and unloading indenting curves in terms of elastic modulus and hardness values at different temperatures. Moreover, the role of heavily deformed non-pinned ultra-fine grains and nano-grains pinned by nano-sized particles

is described in terms of the thermal stability and active softening mechanisms such as grain boundary diffusion or boundary sliding phenomena.

2. Experimental procedure

2.1. Raw materials (foil and powder)

In this research, ~16 µm thick commercial aluminum foil widely used for food packaging implemented as raw material, with a chemical composition determined by inductively coupled plasma-atomic emission spectroscopy (ICP-AES) to be 0.55 *wt%* Mn, 0.25 *wt%* Si, and 1.24 *wt%* Fe, consistent with alloy AA8006. It was sectioned as rectangular samples with a length of 500 mm and a width of 250 mm before application as the starting material. Moreover, B$_4$C nanoparticles with an average size of ~35 nm were purchased from US Nano Company and employed as the reinforcing agent for nanocomposite production. Bright-field transmission electron microscopy (TEM) images from the distribution of such B$_4$C nanoparticles are illustrated in Figs. 1a-c. The relating selected area diffraction (SAD) ring patterns from B$_4$C nanoparticles are shown and indexed in Fig. 1d. High magnification dark-field TEM images showing the individual B$_4$C nanoparticles are demonstrated in Figs. 1e, f. The morphology of nanoparticles seems close to spherical, with a narrow size distribution varied around the average value.

2.2. Implementation of accumulative fold-forging (AFF) process

The AA8006 aluminum alloy foil and B$_4$C nanoparticles were combined via the accumulative fold-forging (AFF) process. The AFF process steps to fabricate the layered ultra-fine grained (UFG) alloy and nanostructured (NS) nanocomposite materials are schematically illustrated in Supplementary Electronic Document, ESI Fig. S1. As shown, the AFF process concept involves repetitive folding of the metallic foil and subsequent forging action to bond the stacked foil layers. To start the process, at first, the initial rectangular foil sample with a dimension of $500 \times 250 \times 0.016$ mm^3 was folded seven times to produce the 128 number of layers with a cross-sectional size of 31.25×31.25 mm^2. Without introducing any reinforcing agent between the multi-layers, the AFF process's result is a layered UFG AA8006 aluminum alloy. However, to synthesize the layered metal-matrix nanocomposites, the incorporation of reinforcing nanoparticles between the layers begins by dispersing these particles in the early folding step. As shown in ESI Fig. S1, B$_4$C nanoparticles were sprayed on the surface of the as-received AA8006 aluminum alloy foil before stacking to form a thin reinforcing surface layer. A stable colloidal solution was prepared for this by dispersing the B$_4$C nanoparticles into an ethanol solution and breaking the aggregates by ultrasonic vibrations for 2 h. The AA8006 aluminum alloy foil was weighted before and after spraying B$_4$C nanoparticles to determine the weight percent or volume fraction of reinforcing agents. In this work, the spraying process and subsequently, the amount of B$_4$C nanoparticles was controlled to attain a volume fraction of ~10% between the layers. After spray deposition of B$_4$C nanoparticles, the foil with a coated B$_4$C layer was placed in an oven, heated at a temperature of ~100 °C, and dried.

The foil was also prepared separately without B$_4$C powder and folded seven times. From this point, AFF process implementation proceeded similarly for both the production of UFG AA8006 aluminum alloy and AA8006-B$_4$C nanostructured nanocomposite materials. After folding the foil layers seven times, the produced multi-layer structure was subjected to standard forging at room temperature to bond the folded sheets chemically/metallurgical. A hydraulic press made by Macrodyne Technologies Company (Canada) with a capacity of 300 tons used for this step. A displacement controlled thickness reduction of ~50% was imposed under the forging action. To continue this fold-forging process for more steps, a 180-degree U-bending from the middle plane of the forged sample was performed. This bending stage is
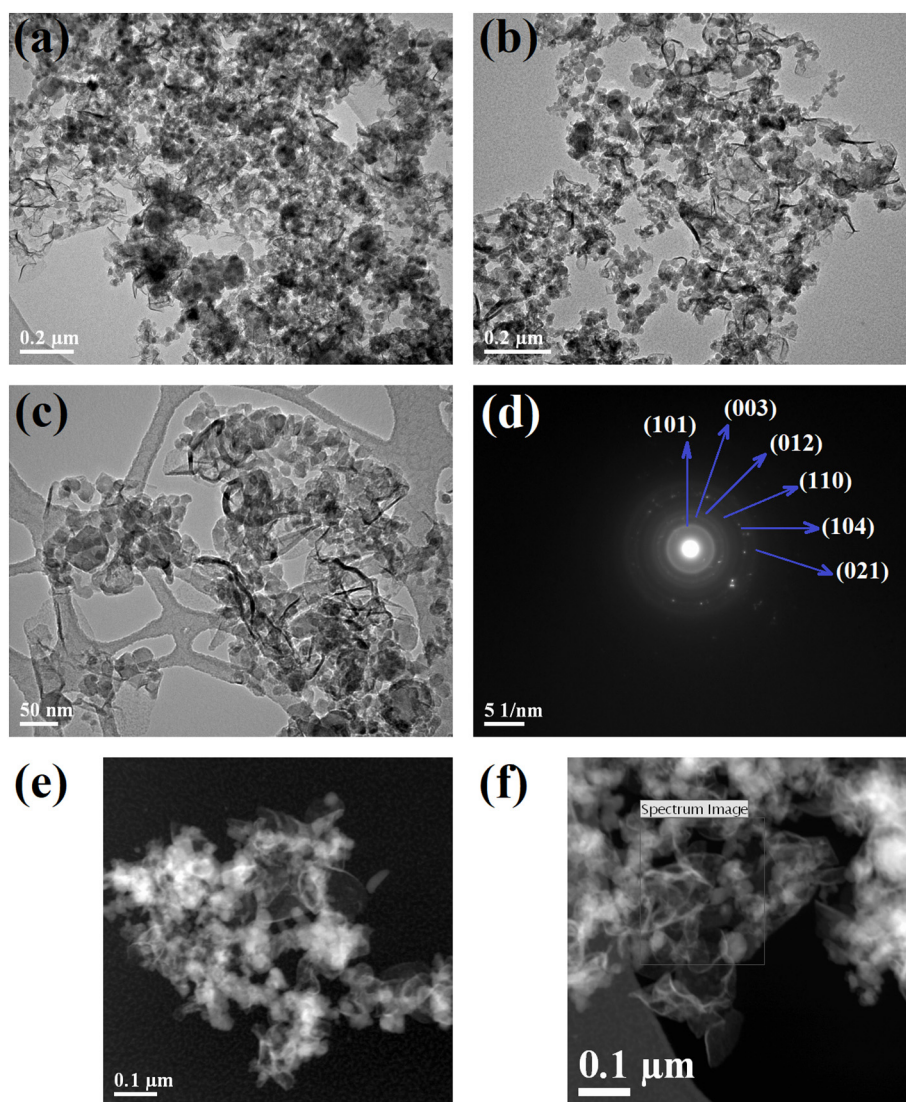
Fig. 1. (a-c) TEM images, (d) SAD ring pattern, and (e, f) STEM images from the B_4C nanoparticles.

very critical in the successful implementation of the AFF process. It was possible for foil samples without reinforcing agents to accomplish that step at room temperature due to the folded layers' lower strength. Meanwhile, for the nanocomposite sample, strength was relatively high, and slight heating up to a low temperature of 150 °C was required to accommodate the U-bending/stacking process (see a schematic of ESI Fig. S1). The two parts of the bent sample were then placed on top of each other, re-folded again, and the forging step was completed to bond them together. The number of layers becomes two-times higher as compared to the previous level after each fold-forging step.

A sample with 67,108,864 number of layers produced with a thickness between 1.5 mm to 2 mm by continuing this AFF process up to 26-steps in a cyclic manner on both the AA8006 aluminum alloy foil and the AA8006-B_4C nanocomposite. In the alloy foil, the formation of millions of layers with a small thickness leads to the generation of an ultra-fine grain structure. On the other hand, incorporating B_4C nanoparticles between such a multi-million number of layers during the AFF process yields to the uniform dispersion of reinforcing agents and a nanostructured nanocomposite formation. The AFF process exhibited great potential for producing homogenous metal-matrix nanocomposites with a high volume fraction of reinforcing nanoparticles. Therefore, in this work, AFF was implemented for the fabrication of a layered

AA8006-B_4C nanostructured nanocomposite with approximately 10 *vol%* of B_4C nanoparticles.

2.3. Microstructural characterization

In this research study, three kinds of samples were prepared according to the AFF process and considered for detailed investigation in terms of microstructural characterization and subsequent micro-mechanical performance. These three categories of samples can be described as; (*i*) first AA8006 aluminum alloy foil, (*ii*) UFG AA8006 aluminum alloy, and (*iii*) AA8006-B_4C nanostructured nanocomposite.

2.3.1. Field emission-scanning electron microscopy (FE-SEM)

The investigation of grain structures and clustering of particles during the dispersion of B_4C nanoparticles was performed by field emission-scanning electron microscopy (FE-SEM). Small specimens were sectioned using the electrical discharge machining (EDM) technique for FE-SEM studies. The standard metallographic sample preparation procedure was carried out by grinding on SiC papers and mechanical polishing on diamond pastes down to a minimum size of ~0.1 μm. A JEOL 7600 (JEOL, Japan) FE-SEM microscope operating at 45 keV was employed to study the polished samples' grain structural features.

2.3.2. Electron backscattering diffraction (EBSD) analysis

Electron backscattering diffraction (EBSD) analysis samples were prepared by chemo-mechanical polishing on OPS suspension (colloidal silica, SiO_2, 20 nm) for 5 min, followed by ion milling (PIPS, JEOL, Japan) using a voltage of 3 keV and current of 1 mA for 2 h. Orientation microscopy investigations were carried out using a JEOL 7600 FE-SEM microscope equipped with an EBSD detector. After re-indexing and plotting the EBSD data, the removal of artifacts was accompanied using the Mambo, Tango, and Salsa software. According to the definition, low-angle grain boundaries (LAGBs) were considered as sub-grains with a misorientation angle in the range of 1.5–15 degrees and high-angle grain boundaries with a higher than 15 degrees. Simultaneous implementation of OPS polishing and ion milling was utilized for the final sample preparation procedure to increase the EBSD index rate. EBSD measurements were successful with an index rate of higher than 85% for the first AA8006 aluminum alloy foil. However, for the AFF processed layered UFG AA8006 aluminum alloy and AA8006-B_4C nanostructured nanocomposite materials, the sample preparation method needed further optimization, considering the 40% indexing obtained was not sufficient for confident EBSD mapping. FE-SEM imaging based on electron channeling contrast was utilized for these samples to study the grain structures. Backscattered electrons were detected for channeling contrast imaging from precipitates, layers, and ultra-fine grains of the aluminum matrix.

2.3.3. X-ray diffraction (XRD) analysis

The X-ray diffraction (XRD) analysis was performed on both processed UFG AA8006 aluminum alloy and AA8006-B_4C nanostructured nanocomposite materials as a complementary method to EBSD analysis to determine the macro-textural evolution during the AFF process. Small rectangular specimens with cross-sectional dimensions of 10×15 mm^2 were prepared from the middle of fold-forged samples by EDM cutting. The standard metallographic sample preparation procedure was implemented on both sides of specimens according to the typical mechanical grinding and polishing routes. A slight chemical etching was performed by immersing them under Keller's chemical reagent for 5 s before measurement to reduce the surface strains and make it possible to attain the sharper peaks. Analyses were conducted in the 2θ angle range of 10–100 degrees using a Phillips diffractometer. In the X-ray set-up, $K\alpha$ radiation from a copper target was used with a wavelength of ~0.154 nm as the incident beam with a scanning speed of 0.01 degrees per 10 s.

2.3.4. Focused ion beam (FIB) and transmission electron microscopy (TEM) studies

It was expected that the intense plastic straining and repetitive fold-forging steps of the AFF process could yield the grain structure refinement of the aluminum alloy matrix to the ultra-fine and nano-scale ranges along with a uniform dispersion of B_4C nanoparticles between the nano-layers. Therefore, an essential experimental section of this research work was to characterize the formation of nano-grains during the AFF process and the distribution and interface of B_4C nanoparticles inside the aluminum matrix. To do so, transmission electron microscopy (TEM) analysis was performed on the layered UFG AA8006 aluminum alloy and AA8006-B_4C nanostructured nanocomposite samples. The
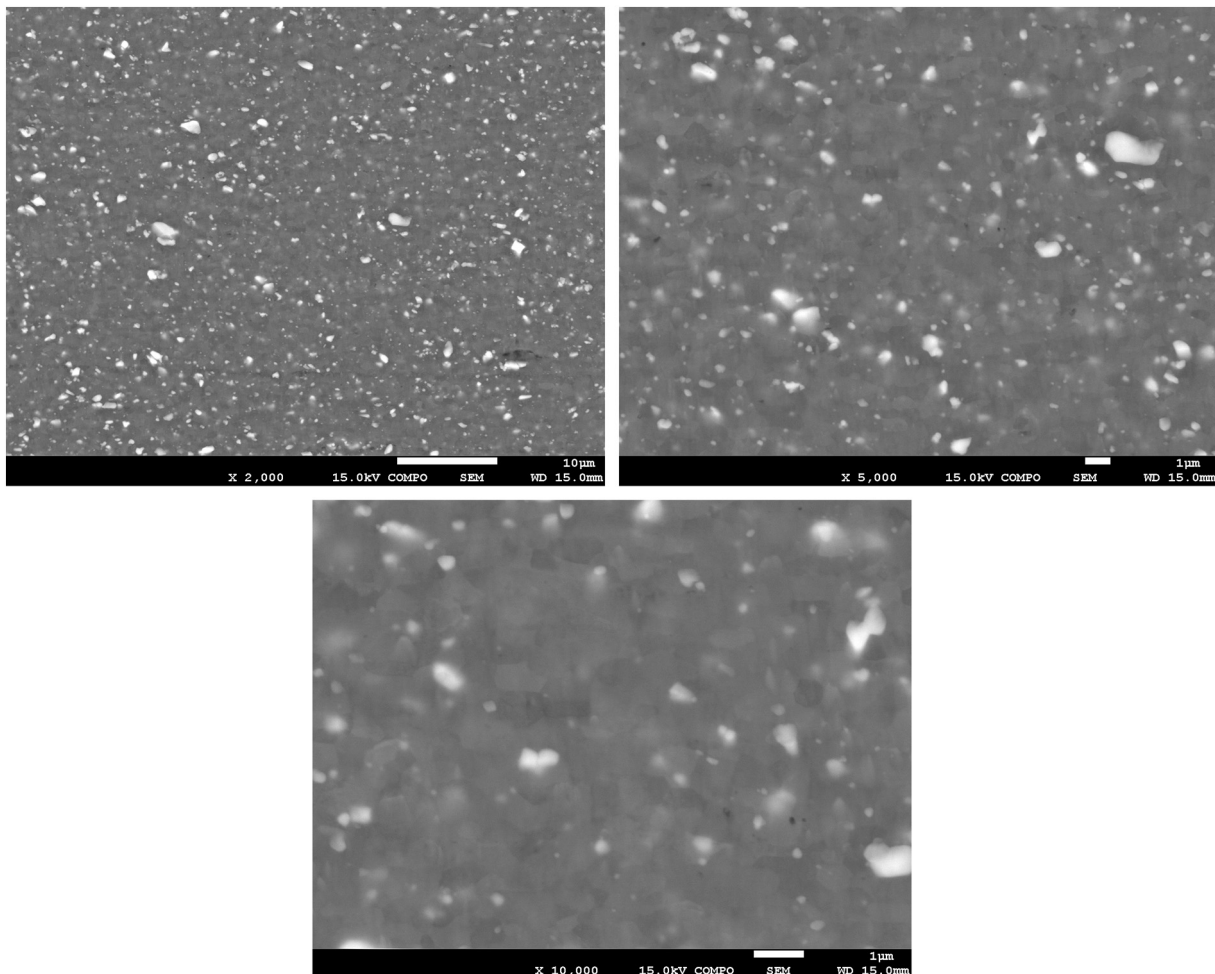

Fig. 2. Channeling contrast FE-SEM images showing the grain structure and precipitates (white-color features) for the initial AA8006 aluminum alloy foil at different magnifications.

focused ion beam (FIB) technique was conducted for sample preparation to extract the thin foils with a thickness of <50 nm perpendicular to the AFF direction. A Zeiss Schottky FE-SEM microscope (Germany) operates at a voltage of up to ~30 keV, and a beam current of up to ~300 nA equipped with a cross/dual-beam NVision-40 FIB gun with a resolution of ~0.7 nm was used for this process. The FIB prepared foils used for observation and characterization via two normal JEOL 2010F (Japan) and high-resolution FEI Titan 80–300 LB (US) TEM microscopes operating at 200 keV and 300 keV, respectively. The distribution of B$_4$C nanoparticles between the nano-layers was investigated via chemical/elemental mapping analysis with the electron energy loss spectroscopy (EELS) analysis detector of the Titan microscope.

2.4. Nanoindentation experiments

After materials characterization, the cross-section thickness of polished metallographic samples was considered for localized mechanical testing at different temperatures using the hot nanoindentation experiments. A KLA nano-indenter (USA) was used by setting the applied loading up to ~100 mN for a holding time of ~5 s in the temperature range of 300 to 523 K. After measurements, in addition to the load-indentation depth flow curves, the average elastic modulus and hardness values were determined according to the Oliver-Pharr approach [35] for a Berkovich shape of indenter tip and reported.

3. Results and discussion

3.1. Microstructural features

3.1.1. Grain structure

3.1.1.1. Initial AA8006 aluminum alloy foil. FE-SEM images showing the channeling contrast grain structure and dispersion of precipitates in the AA8006 aluminum alloy observed in the normal plane are illustrated in Fig. 2. In these images, the white contrast round features correspond to the secondary phase precipitates inside the aluminum matrix. Channeling contrast shows the grain boundaries at high magnifications. The EBSD grain structural maps are shown in Fig. 3, which indicates the first aluminum alloy foil contains fine grains with an equiaxed morphology and a mean size of ~1.04 μm. The average misorientation angle is measured to be around 35.3° with a > 99% fraction of HAGBs. As described in the existing literature of mentioning AA8006 aluminum alloy foils for applications in the food-packaging industry [36,37], such material is processed through a combined manufacturing route including homogenization, rolling, and back-annealing, to achieve such a high degree of thickness reduction through cumulative plastic straining/deformation to produce a thin foil (thickness of less than 16 μm). Therefore, the previous thermo-mechanical history during these processing steps, which involved homogenization and recrystallization, is responsible for forming fine equiaxed grains with high-angle boundaries inside the AA8006 alloy evident in the EBSD data of Fig. 3.

3.1.1.2. Ultra-fine grained AA8006 alloy. The alloy's microstructural features completely changed after implementing the AFF process compared to the as-received aluminum foil. FE-SEM channeling contrast images reveal the grain structure of the aluminum matrix and the distribution of precipitates within the specimen, presented in Fig. 4. Some degree of grain refinement along with a change in the size distribution and morphology of precipitates can be highlighted after the AFF process. Meanwhile, to study the grain structural evolution in more detail, XRD and TEM characterization are required as the principal well-established analysis approaches. XRD patterns from the AFF processed layered UFG AA8006 aluminum alloy and nanocomposite are compared in Fig. 5. Peaks of the aluminum matrix as an FCC metal are labeled on the pattern for the principle diffracting planes (111), (200), (220), (311), and (222). Some small peaks related to the diffraction from fine
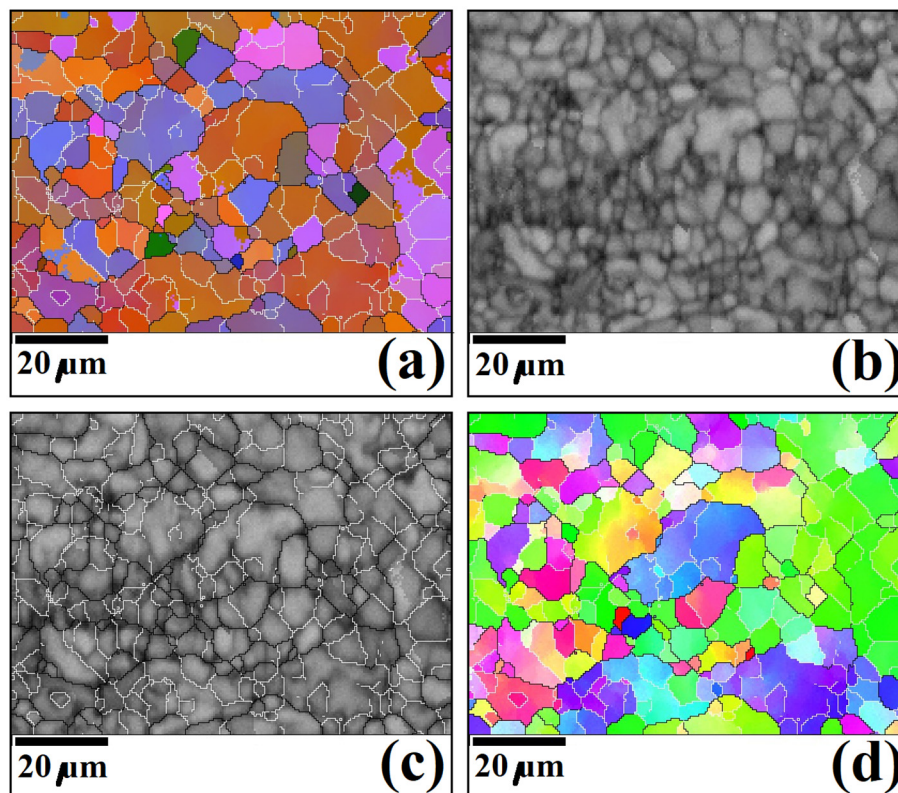
Fig. 3. EBSD analysis results for the initial AA8006 aluminum alloy foil: (a) grain orientation map, (b) grain structural map, (c) grain boundary map, and (d) inverse pole-figure grain structural map.
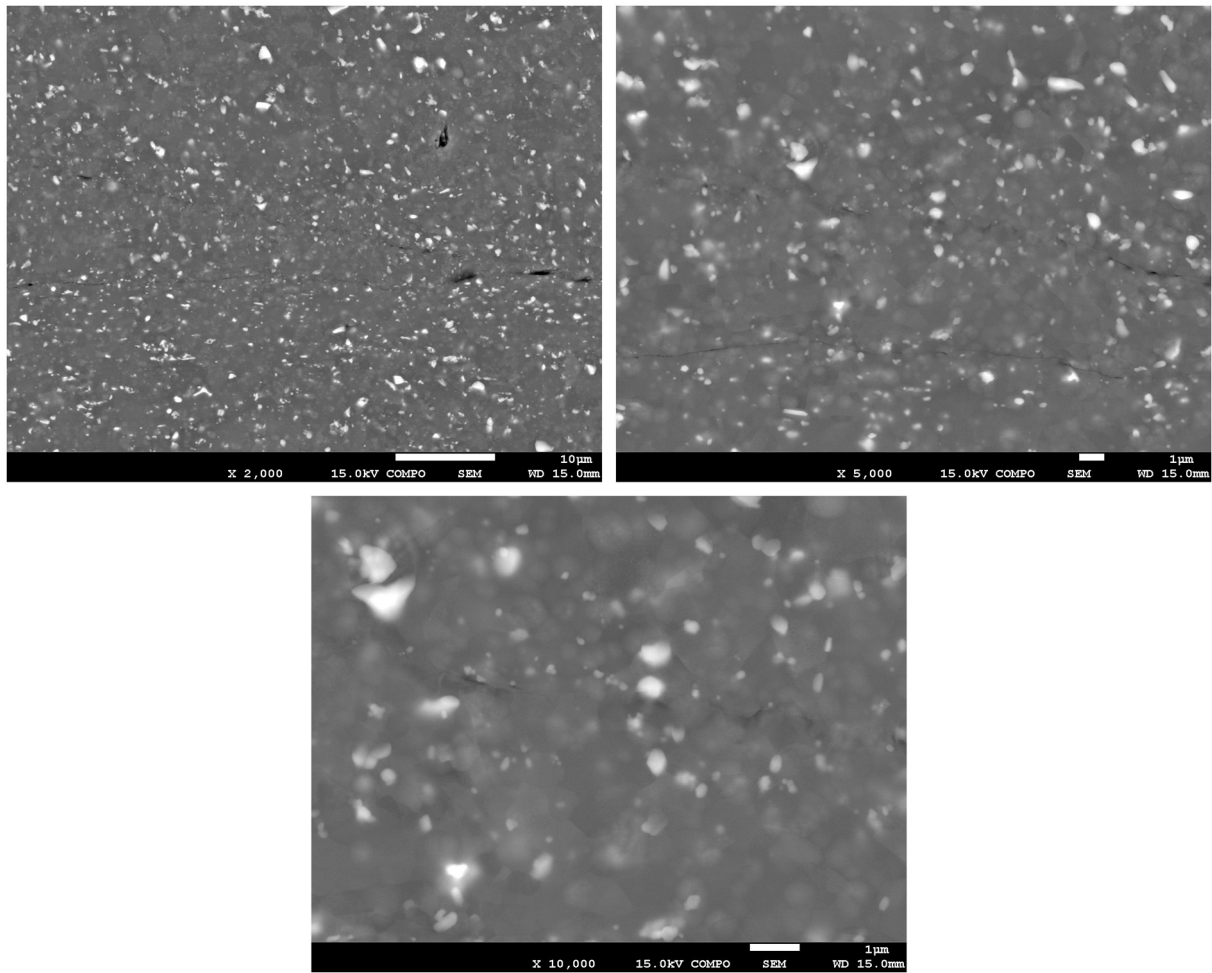
Fig. 4. Channeling contrast FE-SEM images showing the grain structure and precipitates (white-color features) for the UFG AA8006 aluminum alloy at different magnifications.

precipitates can be indexed as well. Based on the X-ray diffraction peaks broadening and measuring the full-width at half maximum (FWHM), it would be possible to estimate the average cell size and mean dislocation density [38,39]. Using the modified Williamson-Hall approach [40,41], these values were calculated around 200 nm and 7.2×10^{15} m^{-2}, respectively, in the processed UFG AA8006 aluminum alloy. The FIB/TEM

Fig. 5. XRD patterns for UFG AA8006 aluminum alloy and nanostructured AA8006-B$_4$C nanocomposite.

analysis was implemented as a direct observation to confirm the indirect measurements demonstrated in ESI Fig. S2. Both bright-field (BF) and dark-field (DF) contrast images are illustrated. Based on these TEM images, the formation of ultra-fine grains with an average size of ~200 nm via severe plastic straining of the AFF process can be confirmed. The UFG structure is slightly elongated perpendicular to the forging direction along the radial axis. Furthermore, in the top BF images, precipitates can be traced by the presence of grey-contrast features, as well as the white-contrast features in the bottom DF images. The structure of these round precipitates will be further characterized in the next sections.
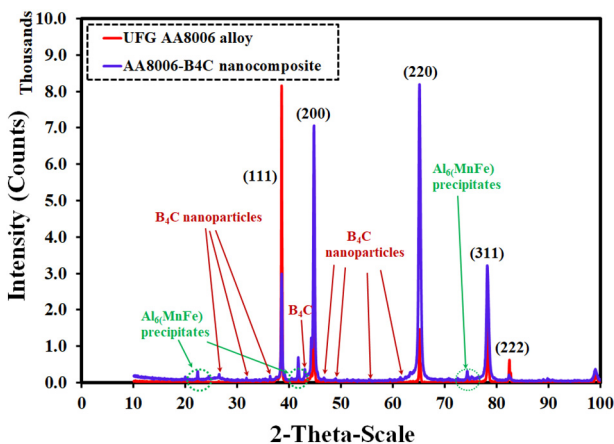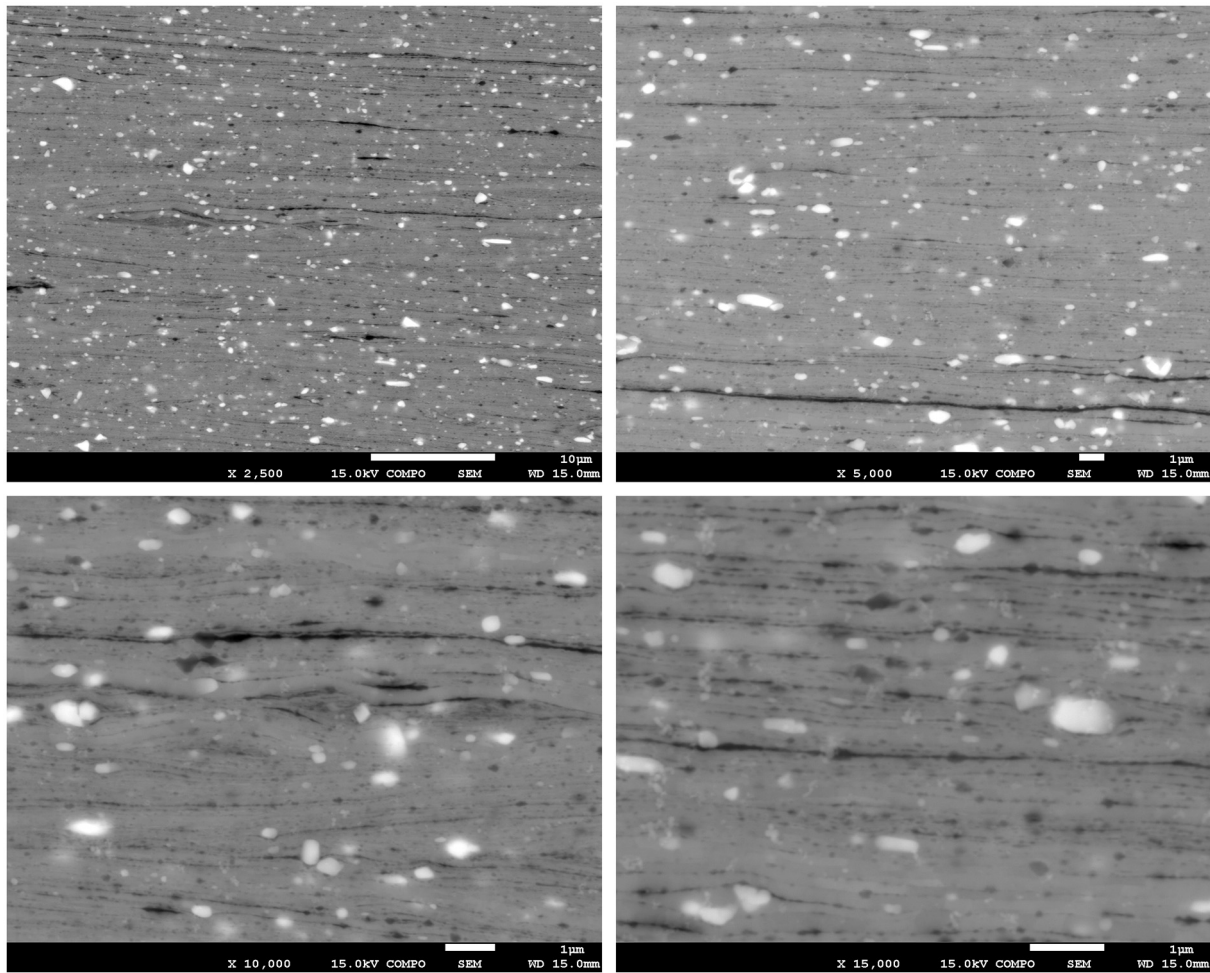
3.1.1.3. AA8006-B$_4$C nanostructured nanocomposite. FE-SEM images from the structure of layers and dispersion of reinforcing B$_4$C nanoparticles between the nano-layers are illustrated in Fig. 6. In this FE-SEM analysis, the focus was on imaging using electron channeling contrast. Meanwhile, it seems that the grain structure of the aluminum matrix for this nanocomposite sample was considerably refined to value even below the detection limit of the scanning microscope. In the FE-SEM images, the presence of nano-layers and the dispersion of clusters of B$_4$C nanoparticles (with dark contrast) inside the aluminum matrix are visible. The precipitates are the white contrast round features. The XRD pattern for the AA8006-B$_4$C nanocomposite is demonstrated in Fig. 5. In this new pattern, in addition to the peaks of aluminum and precipitates, some small peaks show the presence of B$_4$C nanoparticles within the aluminum matrix. The average size of grains and the mean density

Fig. 6. Channeling contrast FE-SEM images showing the grain structure, precipitates (white-color features), layers (black-color directional lines), and reinforcing nanoparticles (black-color features) for the nanostructured AA8006-B$_4$C nanocomposite at different magnifications.

of total dislocations for the AA8006-B$_4$C nanostructured nanocomposite were determined according to the XRD approach as ~35 nm and ~ 8.1×10^{16} m^{-2}, respectively. Direct observation based on TEM analysis was performed to characterize the microstructural features in the real state. The FIB/TEM images at high magnifications for the processed nanocomposite perpendicular to the AFF direction are presented in Fig. 6. Formation of such nano-sized grains/cells for the aluminum matrix after the AFF process, as indexed before based on the XRD peaks broadening, can be validated considering these high resolution-TEM images. Nano-grains are slightly elongated in the radial direction perpendicular to the fold-forging direction, with a rectangular morphology. The existence of round precipitates as the grey-contrast features surrounded by the nano-grains as well as the distribution of B$_4$C nanoparticles corresponding to the dark-contrast elements between the nano-layers are apparent in the TEM images of Fig. 6.

3.1.2. Crystallographic texture

One of the novel objects of this article deals with the implementation of electron backscattering diffraction (EBSD) and X-ray diffraction (XRD) analyses for the first time on the AFF products to characterize the grain refinement and crystallographic textural evolution during layer-upon-layer bonding without the alloy and in the presence of B$_4$C nanoparticles as a reinforcing agent. The inverse pole-figures (IPFs), pole-figures (PFs), 3D map of orientation distribution function (ODF), and 3D illustration of significant components inside the examined area based on EBSD analysis on the as-received AA8006 aluminum

alloy foil is plotted in Figs. 7a-d, respectively. Analysis of the crystallographic textural components reveals the contribution of a strong directional preferred orientation, with a high J-index of ~5.7, due to the deformation imposed during material processing in the cumulative drawing and annealing treatments. According to these pole-figures in Fig. 7, the typical recrystallization textures of FCC metals and alloys in the form of cube and brass components mixture can be indexed, as well.

After the AFF process on the alloy and then incorporating B$_4$C nanoparticles, the average size of produced ultra-fine and nano-grains was considerably below the detection limit of EBSD analysis. Hence, as explained in the experimental procedure section, indexing and grain structural mapping, as well as the textural plots, were not successful. Therefore, these two processed materials' crystallographic texture could only be measured based on the macro-scale XRD analysis shown in Fig. 5. However, elongation of ultra-fine and nano-grains along the radial direction perpendicular to the fold-forging direction is illustrated before in high-magnification TEM images of ESI Figs. S2 and S3, we can note the presence of some micro-scale and nano-scale preferred orientations after AFF processing. Such microstructural features exhibited the altered crystallographic texture at the macro-scale as well. It can be highlighted in the XRD patterns of Fig. 5 that changes in the intensity of the diffracted peaks in addition to the related ratios. In the UFG state, without incorporating any reinforcing agent, the maximum diffraction intensity is associated with the close-packed planes based on the higher multiplicity factor of (111) planes for FCC metals. After introducing the B$_4$C nanoparticles between the nano-layers and
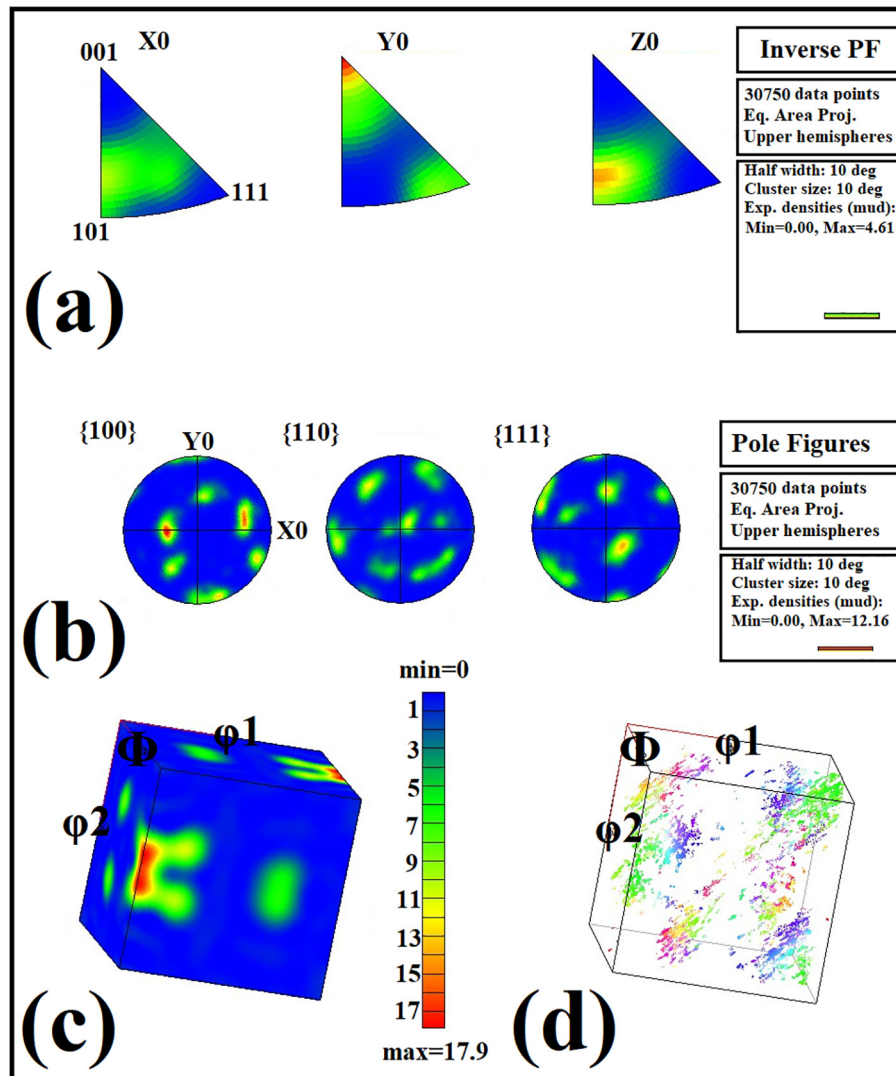
Fig. 7. (a) Inverse pole-figure (IPF) plots, (b) orientations of {100}, {110}, and {111} as the pole-fig. (PF) plots, (c) 3D plot of orientation distribution functions, and (d) 3D plot of inside components for the primary AA8006 aluminum foil alloy before AFF treatment.

the production of AA8006-B_4C metal-matrix nanocomposite, the intensity of the (111) diffraction peaks are considerably reduced, and two new diffraction planes of (200) and (220) reach the maximum intensity. These signals approve the dominance of new preferred crystal orientations.

3.1.3. Secondary phase precipitates

As described in the experimental procedure section based on ICP characterization, the content of Fe and Mn in the alloy is near to the ternary eutectic composition. According to the specification for AA8006 alloy, which calls for mainly Fe and Mn additions, and minor Si content, as well as intense thermo-mechanical action during foil processing (rolling to a thickness less than one hundred micron and subsequent annealing treatment), this leads to two types of secondary phase precipitates via solid-state phase transformations [36,37]. Due to aluminum and iron elements' high chemical reactivity to form iron aluminide, there is a high driving force to develop the intermetallics $FeAl_6$ and $FeAl_3$ during alloy processing. However, the stability of these phases can be affected by the solid-state diffusion and solubility of the Mn element. Different Fe: Mn ratios from 5.9:1 to 42:1 can lead to the generation of other phases which substitute Mn in the lattice, including $(Fe, Mn)Al_6$ and $(Fe, Mn)Al_3$, respectively [36]. Also, some other

intermetallic phases such as; AlFe, AlMn, and AlFeMnSi may form, depending on the following issues: (*i*) solidification cooling rate, (*ii*) addition of agents at the microscale, (*iii*) total Fe, Si, and Mn content, and (*iv*) refining of the grain structure during treatment [36]. Such intermetallic phases significantly affect the mechanical properties of the final products based on AA8006 aluminum alloy.

An exciting combination of mechanical properties in terms of tensile strength and elongation to failure was noted for this AA8006 alloy in the literature [36,37]. Moreover, this alloy can maintain its mechanical strength at elevated temperatures. This behavior's structural aspect is based on the pinning of a fine grain structure produced during thermo-mechanical treatment via an elegant and stabilized distribution of secondary phase precipitates [36,42]. Therefore, characterizing the nature and morphology of such intrinsic particles as well as their dispersion through the aluminum matrix after AFF treatment is a critical issue in determining their role in plasticity at the micro- and nano-scales. This is explored in terms of the thermal dependant response of depth-sensing indentation in the AFF processed AA8006 alloy and AA8006-B_4C nanostructured nanocomposite.

Dark-field TEM images indicate the distribution of different precipitates through the aluminum alloy matrix after AFF processing, while the selected area diffraction (SAD) spot pattern confirms the presence of
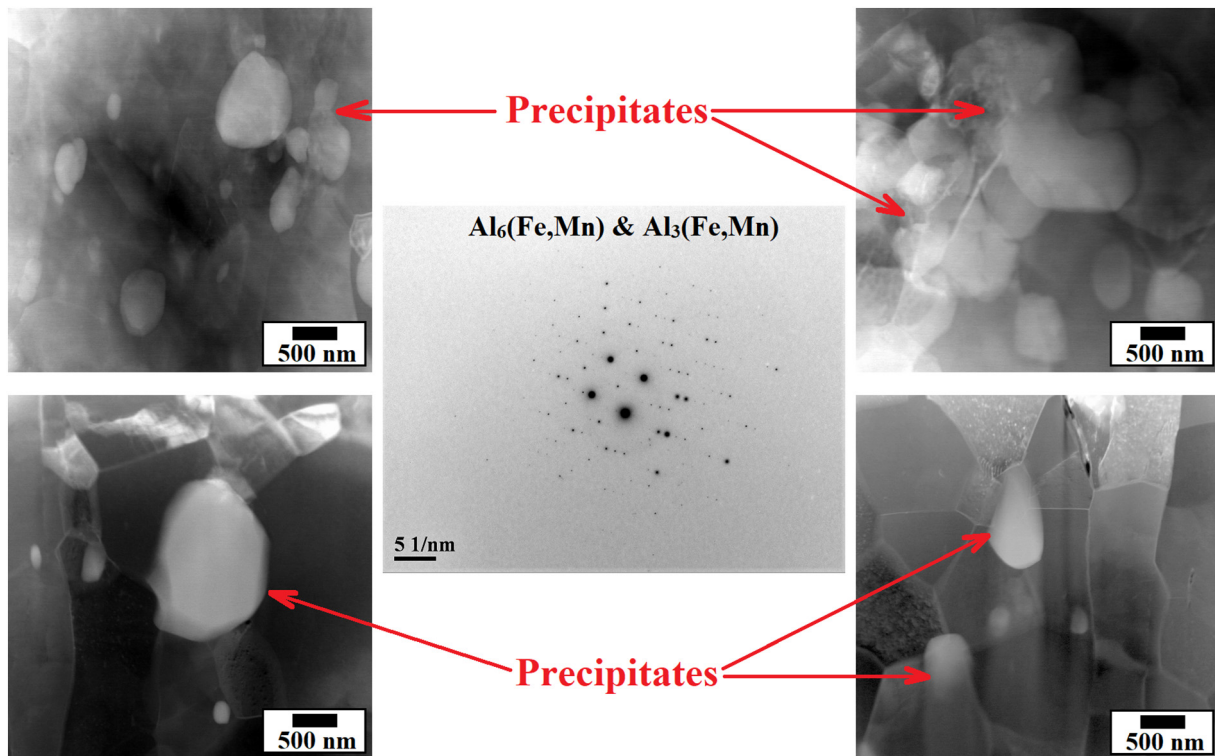
Fig. 8. HAADF and DF-STEM images, as well as the SAD pattern from precipitates. White-color contrast features illustrating the secondary phase precipitates.

multiple precipitates in Fig. 8. According to these results, precipitates are highlighted by white-contrast features. In a general examination based on these TEM images, two types of large and small precipitates with round (close to spherical) morphology can be noted. The average size of large precipitates was determined by image analysis to be around 0.9 μm, with a volume fraction of ~0.8%. These values can be calculated as ~0.5 μm and 3.5 *vol%* for the fine precipitates, respectively. By indexing the SAD pattern in Fig. 8, along with elemental mapping analysis via the EELS technique, the chemistry, and stoichiometry of large precipitates, were determined to be $(Fe, Mn)Al_3$, and small particles were found to be $(Fe, Mn)Al_6$. In this case, the elemental mapping analysis results attained by TEM and EELS analysis reveals two kinds of fine precipitates, as demonstrated in Fig. 9. The distribution of iron and manganese elements inside such small secondary phases through the aluminum matrix is evident. To distinguish between $(Fe, Mn)Al_3$ and $(Fe, Mn)Al_6$ phases, in addition to crystallography by SAD pattern identification, point elemental analysis was helpful to calculate the related ratios between Fe and Mn elements confirm the elemental concentration is close to the expected stoichiometry.

3.1.4. Dispersion of nanoparticles

The effectiveness of AFF as a new SPD process in terms of the capability to produce a homogenous dispersion of reinforcing nanoparticles with a high volume fraction is striking. In this experimental work, aluminum matrix nanocomposite fabrication's main goal was to incorporate ~10 *vol%* of B_4C nanoparticles to manufacture a nanostructured nanocomposite material. High magnification TEM images from the distribution of reinforcing B_4C nanoparticles between aluminum foil layers are illustrated in Fig. 10. B_4C nanoparticles can be identified as the grey contrast round features in these TEM images, and a white difference distinguishes complex precipitates due to their higher atomic number contrast. Excellent and homogenous dispersion of discrete B_4C nanoparticles with a rather high fraction of ~10 *vol%* can be noted between the nano-layers in the high magnification TEM images. Furthermore, the SAD ring pattern from an area, including B_4C nanoparticles, is
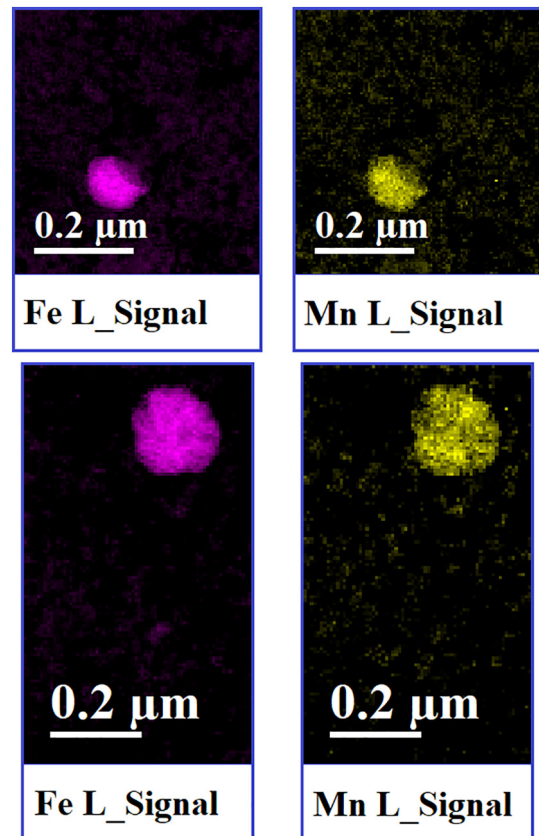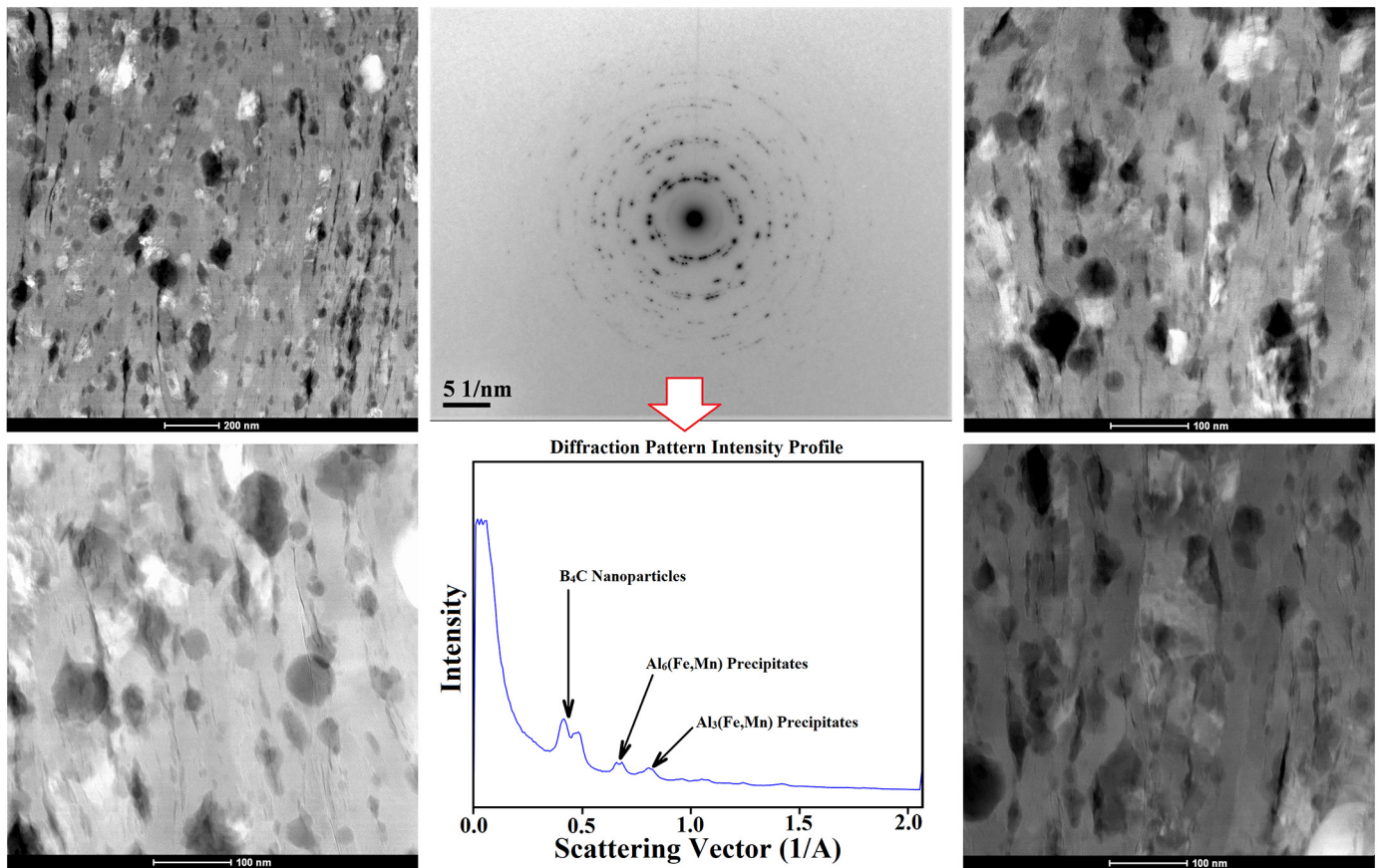

Fig. 9. EELS elemental mapping analysis results from the dispersed precipitates through the aluminum alloy matrix.

Fig. 10. STEM images and SAD patterns for incorporated B_4C nanoparticles between the layers. White-color features showing the precipitates and grey-contrast round fine features demonstrating the B_4C nanoparticles.

illustrated in Fig. 10, where the crystallographic-based analysis confirms the presence of nanoparticles and precipitates within the aluminum matrix in the bright field images. Averaging software was used to sum the ring intensities and generate the intensity profile, which more clearly confirms the presence of scattering vectors associated with B_4C, $Al_6(Fe, Mn)$, and $Al_3(Fe, Mn)$ particulates.

The elemental mapping analysis results from the dispersed reinforcing B_4C nanoparticles between aluminum foil layers by EELS analysis at high magnifications are shown in Fig. 11. Sharp concentrations of boron and carbon are associated with the aluminum matrix's boron carbide phase locations. Moreover, in the EELS maps, the infiltration of oxygen as a significant element at the interfaces between layers and boundaries of the second phase particles can be detected, indicating the presence of aluminum oxide nanoparticles nano-layers. Such new phases are attributed to the initial oxide layer on aluminum foil's surface and its breaking during subsequent fold-forging steps followed by successive uniform dispersing between several million layers. Beside the B_4C nanoparticles (~35 nm, 10 vol%) and complex precipitates with designations of $(Fe, Mn)Al_6$ (~0.5 μm, 3.5 vol%) and $(Fe, Mn)Al_3$ (~0.9 μm, 0.8 vol%) as noted before, such new nano-sized alumina particles are evenly distributed at the interfaces, which may also function as a reinforcing or strengthening agent for the aluminum matrix. Based on EELS results' image analysis, the volume fraction of these Al_2O_3 nanoparticles can be estimated at around 2% with an average size of ~4 nm.

3.2. Hot nanoindentation responses

3.2.1. Load-depth sensing behavior

The nanoindentation testing results related to the load-depth sensing response from the surface section of the first AA8006 aluminum
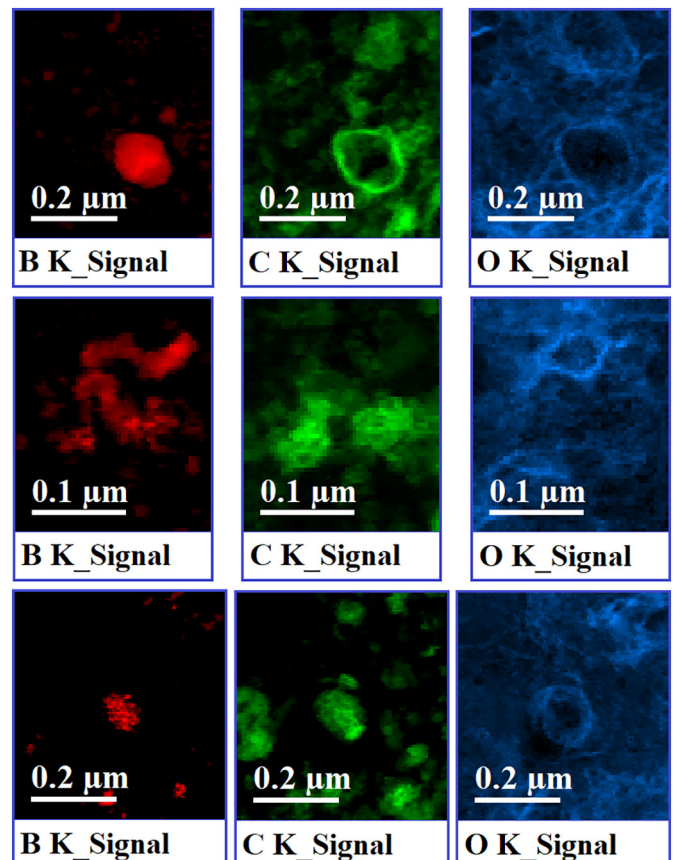
Fig. 11. EELS elemental mapping analysis results from the boron carbide and aluminum oxide nano-sized reinforcing agents through the aluminum alloy matrix.

alloy foil as well as the AFF processed UFG AA8006 aluminum alloy, and AA8006-B$_4$C nanostructured nanocomposite materials were measured for elevated temperatures up to ~523 K and compared to the room temperature responses in Figs. 12–14, respectively. Several measurements were performed under each hot nanoindentation testing condition to confirm the repeatability of results considering the small area and deformation zone during nano-indenting.

For all samples, increasing the testing temperature from room medium to ~523 K reveals an indenting depth, which continuously increases to the maximum loading. Moreover, the fluctuation in load-displacement indenting curves displayed an increasing trend, with a severity that depends on the material. Based on these graphs, it can be emphasized that the UFG AA8006 aluminum alloy exhibited unstable behavior under hot nanoindentation testing with a high degree of fluctuation in the indention response as the testing temperature increases. This behavior is related to the structural restoration occurring in the UFG alloy with increasing the temperature, as discussed in the next sections. However, the indentation response suggests excellent repeatability for the initial foil and nanostructured nanocomposite materials, showing the more uniformity in microstructural development and micro-mechanical properties at elevated temperatures.

3.2.2. Theory and formulation of nanoindentation

The load-displacement ($L-h$) plots in Fig. 15 show the nanoindentation flow behaviors of AFF processed UFG AA8006 aluminum alloy and AA8006-B$_4$C nanostructured nanocomposite materials compared to the initial AA8006 aluminum alloy foil during the loading and unloading stages. These analyzed, according to the model proposed by Oliver and

Pharr [35], where the indentation hardness and elastic modulus of material during indentation testing, can be estimated using the relation below:

$$H_{ind} = \frac{L_{max}}{A_{proj}} \tag{1}$$

where L_{max} is the peak load and A_{proj} is representing the actual contact area. The indenter's projected surface area can be approximated based on the unloading stiffness at maximum loading ($S = \frac{dL}{dh}\big|_{L=L_{max}}$, in Fig. 15), employing the following expressions [35,43]:

$$h_c = h_{max} - \varepsilon \frac{L_{max}}{S} \tag{2}$$

$$A_{proj} = 24.5 h_c^2 + \sum_{i=1}^{8} C_i h_c^{(0.5)^{i-1}} \tag{3}$$

where h_{max} is the total depth (as shown in Fig. 15) and ε is a geometrical constant depending on the shape of the indenter ($\sim \frac{2(\pi-2)}{\pi}$ for a conical Berkovich indenter [35]). Moreover, the elastic modulus during nanoindentation testing can be calculated using the below equation [43]:

$$\frac{1-\upsilon^2}{E} = \frac{1}{E_r} - \frac{1-\upsilon_i^2}{E_i} \tag{4}$$

where E, E_r, and E_i are the elastic modulus of material under indentation testing, the reduced elastic modulus, and the elastic modulus of the indenter, respectively. Also, υ and υ_i are the Poisson's ratios for the specimen and indenter, respectively. The values of E_i and υ_i can be estimated
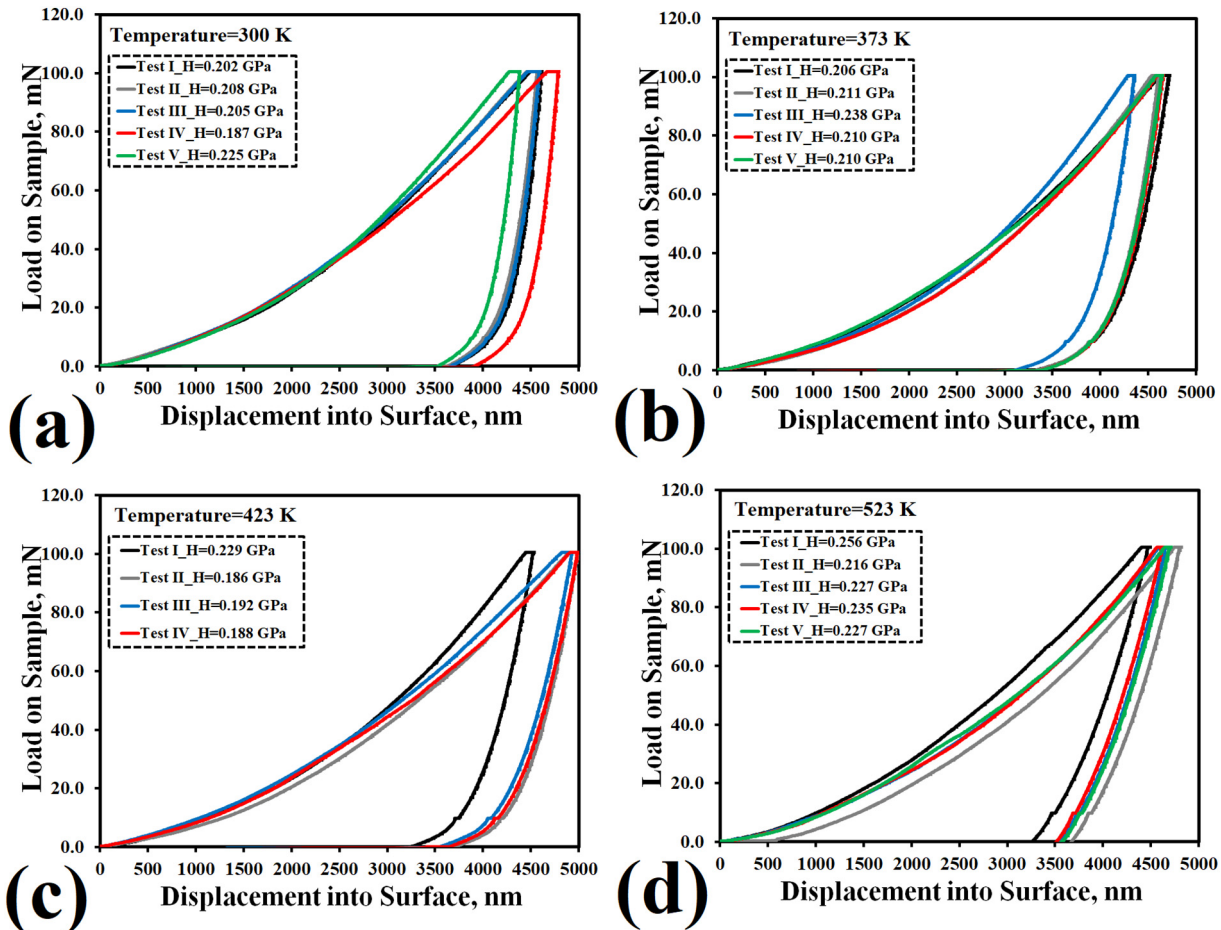

Fig. 12. Indentation load-depth curves for the first AA8006 aluminum alloy foil at different temperatures: (a) 300 K, (b) 373 K, (c) 423 K, and (d) 523 K.
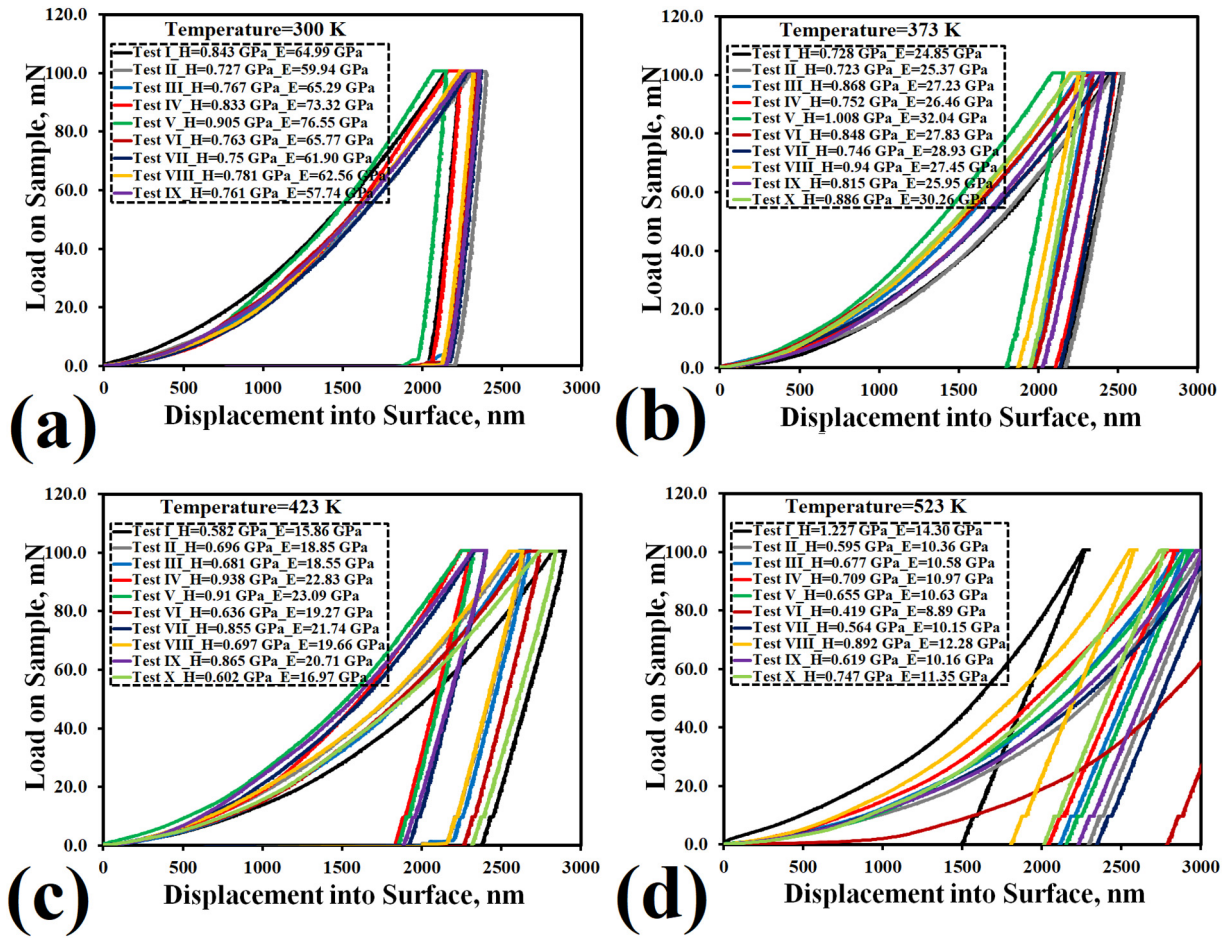
Fig. 13. Indentation load-depth curves for the UFG AA8006 aluminum alloy at different temperatures: (a) 300 K, (b) 373 K, (c) 423 K, and (d) 523 K.

at around 1140 GPa and 0.07 for a diamond indenter. Moreover, the reduced elastic modulus value is defined based on the projected contact surface and stiffness of the unloading curve, according to the following equation [43].

$$E_r = \frac{S}{2}\sqrt{\frac{\pi}{A_{proj}}} \tag{5}$$

The indentation hardness and elastic modulus trends, as illustrated in Figs. 16 and 17 were determined using the above expressions.

3.2.3. Dependency of elastic modulus and hardness on the temperature

By evaluating the load-depth responses in Figs. 12-14, considering the indentation depth under maximum loading as well as the loading and unloading rates, two central distinguishing micro-mechanical properties are calculated in terms of elastic modulus and indentation hardness for various temperatures. Based on these measurements, the average values for the elastic modulus and hardness properties are plotted as a function of indenting temperature in Figs. 16 and 17, respectively. For all materials under investigation, both properties have simultaneously deteriorated at higher temperatures. This is attributed to the weakening of the stiffness with increasing temperature due to an incremental increase of atomic spacing upon expansion and the corresponding reduction of the atomic force vs. displacement curve derived from the Condon-Morse curve [44]. According to the presented data, elastic modulus' dependence on temperature is much more severe than the indentation hardness, mainly due to Young's modulus role on

the required shear stress dislocation glide based on the Peierls Nabarro stress [45–47].

A considerable reduction in the UFG AA8006 aluminum alloy's elastic modulus can be noted with indenting temperature in the range of 300–523 K, illustrating a desirable thermal unstable behavior. This drastic reduction is from ~66.3 ± 5.8 at room temperature down to ~11.0 ± 1.5 at a high temperature of 523 K (see Fig. 16). The incorporation of reinforcing B_4C nanoparticles inside the matrix led to enhanced thermal stability in the structure, allowing it to retain elastic strength at high temperatures better. The role of nanoparticles involves reinforcing nano-sized grains as dislocations-obstacles interactions and the pinning of boundaries or reducing their interfacial energies [48–50]. The slope indicates thermal softening is reduced in the nanocomposite, with a higher elastic modulus value of ~18.3 ± 0.9 GPa at the maximum test temperature. In indentation hardness, the values in Fig. 17 indicate the softening trend is also decreasing; however, the severity is considerably lower. This new development could be attributed to the reduced impact of structural restoration mechanisms in the grain structure and their mitigated impact on the hardness than the elastic modulus since the only possible microstructural phenomenon during low-temperature nano-indenting would be the rearrangement of the dislocation structure according to DRV [51–53]. The highest test temperature of 523 K is below the aluminum alloy's recrystallization temperature, although very close to the heavily plastic deformed structure. No considerable change in indentation hardness is noted for the initial aluminum foil alloy, while about 11% and 30% reductions occur in the UFG alloy and nanostructured nanocomposite materials as the temperature reaches 523 K. As shown in Fig. 17, the indentation hardness of AA8006-B_4C
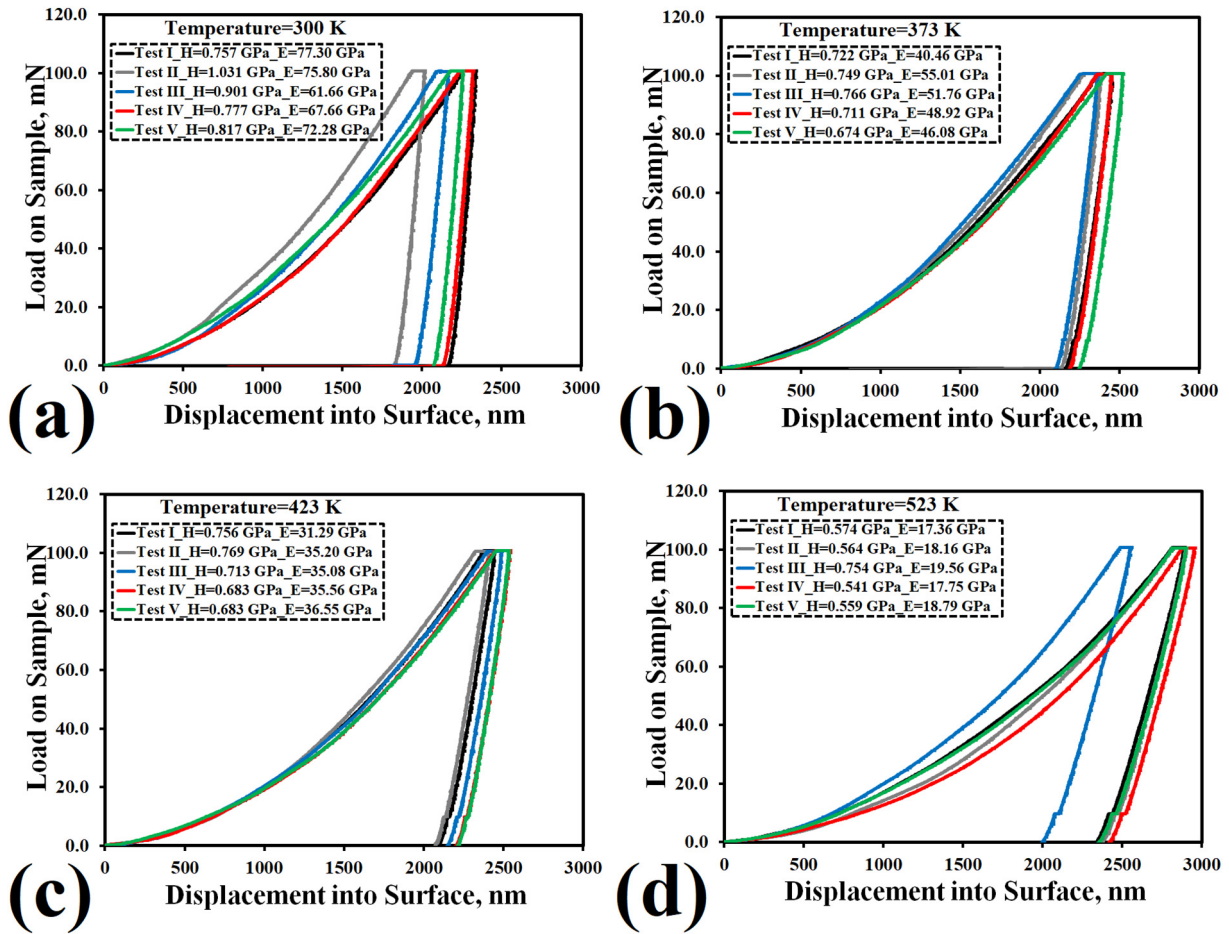
Fig. 14. Indentation load-depth curves for the nanostructured AA8006-B$_4$C nanocomposite at different temperatures: (a) 300 K, (b) 373 K, (c) 423 K, and (d) 523 K.

nanostructured nanocomposite is higher at room temperature than expected UFG AA8006 aluminum alloy due to the incorporation of reinforcing B$_4$C nanoparticles along with the formation of ultra-fine and nano-grains. However, during nano-indentation testing at elevated temperatures, the trend of average hardness variation for UFG alloy in some points displayed an increasing manner compared to the room temperature state. In the case of UFG alloys produced by SPD processes,

their stability upon subsequent thermal heating phenomena is a critical issue considering the active dynamic restoration mechanisms. For severely plastic deformed aluminum and its alloys, experiments revealed a slight improvement in mechanical strength upon exposure to low-temperature annealing treatment below the critical recrystallization point. This unexpected behavior results from competition between restoring and rearrangement of statistical and geometrically necessary
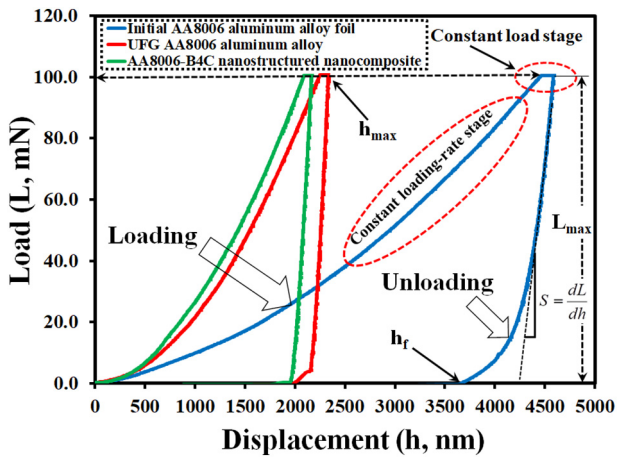

Fig. 15. Comparison between the typical force-depth response showing different stages for the initial AA8006 aluminum alloy foil, UFG AA8006 alloy, and AA8006-B$_4$C nanostructured nanocomposite during nanoindentation testing at room temperature.
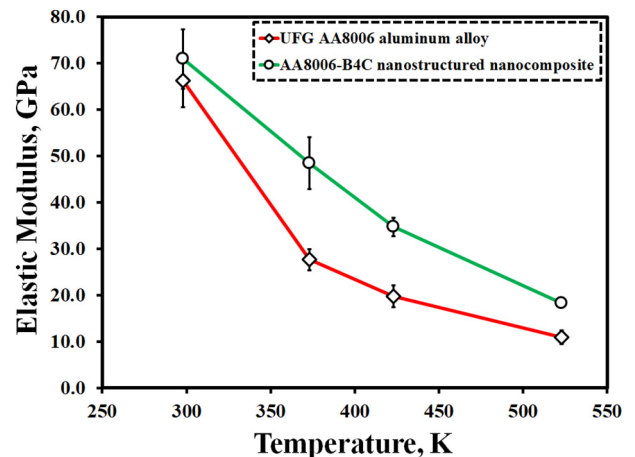

Fig. 16. Variations of mean elastic modulus data versus indenting temperature for the processed materials.
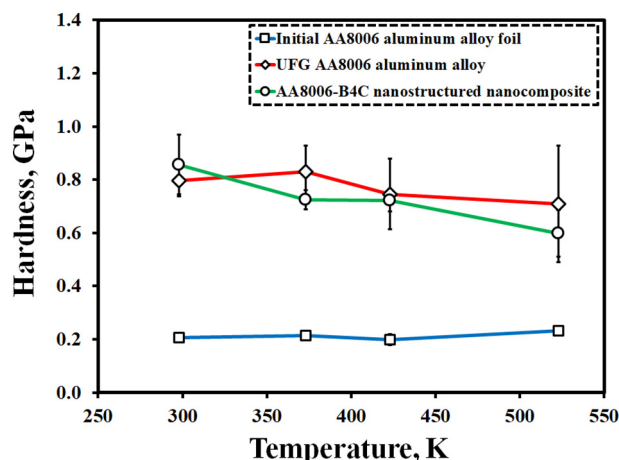
Fig. 17. Variations of mean indentation hardness values versus loading temperature for the started and processed materials.

dislocations and the generation of the nucleus for new grain. The same trends were also reported previously for aluminum alloys by other SPD routes upon thermal annealing after severe plastic deformation [54,55].

3.2.4. Thermal softening property

The change in the slope of loading and unloading curves, along with the maximum penetration depth under the constant loading stage, further reveals the thermal softening response of the processed materials. In this context, Fig. 15 illustrates the comparison between indentation load-displacement curves of the first AA8006 aluminum alloy foil, UFG AA8006 aluminum alloy, and AA8006-B_4C nanocomposite, measured nanoindentation at room temperature. The higher slope of the loading and unloading stages observed in the UFG alloy and nanocomposite than the primary alloy is correlated to these materials' higher stiffness. To explain the thermal softening by nanoindentation testing, the indentation curves' slope must be recorded at varying test temperatures, as shown in Figs. 12–14. Lower reductions in the stiffness of the material indicate higher thermal stability. As the decline rate in the slope with temperature was insignificant in the first foil, this suggests high thermal stability. The coarse grain structure of the aluminum foil stabilized after recrystallization supported by the role of fine precipitates. However, the initial alloy's stiffness values were the lowest, considering the low strength of the material structure. Meanwhile, the temperature-sensitive trend for the slope of loading and unloading curves was noted for the UFG AA8006 aluminum alloy, mainly due to the presence of unstable sub-grains within the ultra-fine structure, contacting a high density from the statistical and geometrically necessary dislocations after the severe strains involved in the AFF process. The exciting feature of the trends in Figs. 12–14 is a reduction in the rate of softening developed by the incorporation of B_4C nanoparticles. Such a drop in the slope signifies a considerable enhancement of thermal resistance for the nanocomposite material caused mainly by reinforcing B_4C nanoparticles' pinning action to restrict grain boundary migration and coalescence of nano-grains. In the case of these fold-forged layered composite materials, it would be quite challenging to conduct tensile flow testing because of dimensional limitations, although the possible results and trends could be quite attractive and practical. However, considering the localized micromechanical properties in terms of indentation hardness and elastic modulus as reported in this research, the tensile strength of processed materials can be estimated based on the established general correlations developed in the literature. Moreover, the exciting property to examine for future studies could investigate the damping capacity across the layered structure perpendicular to the thickness section that requires resonance testing [56,57].

4. Conclusions

Formation of a layered structure containing the ultra-fine grains with an average size of ~200 nm and a developed mean dislocation density of ~7.2×10^{15} m^{-2} noted as a result of the AFF repetitive fold-forging process on the initial AA8006 alloy foil. After incorporating reinforcing nano-sized B_4C particles between the nano-layers, characterization revealed further grain structure refinement to the nano-scale range of ~35 nm with an enhanced dislocation density to ~8.1×10^{16} m^{-2}. Depth-sensing thermal stability of processed materials in the form of layered UFG alloy and nanostructured nanocomposite under nanoindentation testing reported quite different behavior than the initial alloy foil tested at different temperatures. Refining the grain structure into the UFG range imparted an admirable influence on reducing the indentation depth under constrained loading, which means the surface's higher strength. In contrast, indentation curves revealed that by elevating the temperature, lower strength with a substantial fluctuation of data occurred on the nanoindenter location and heterogeneous grain coarsening phenomenon. Introducing nanoparticles and other grain structural refinement into the nano-scale range introduced additional enhancement of localized strength, showing the lower indentation depths, i.e., higher localized resistance, with more thermally stable behavior. Elastic modulus and hardness values determined in correlation to material stiffness based on the loading and unloading curves during nanoindentation revealed the declining trends with increasing testing temperature. The elastic modulus of the UFG alloy suddenly dropped with elevating temperature from an initial value of ~66.3 GPa down to ~10.9 GPa at a temperature of 523 K (a reduction of ~84%), attributed to the high sensitivity of the severely deformed structure upon heating and rearrangement of dislocations by the DRV mechanism during low-temperature nanoindentation. However, the nanostructured nanocomposite material demonstrated a more stable behavior with a lower elastic modulus, which decreased by only ~74% due to nanoparticles' presence as obstacles against dislocations and pinning sites the grain boundaries. The indentation hardness trend reflected the same thermal softening manner. However, the softening rate was considerably lower than the elastic modulus (~30% at the maximum state), caused by noteworthy grain structure restoration during hot nanoindentation testing through the low-temperature range.

Credit author statement

Considering the exceptional chemical, physical, functional, and mechanical characteristics of ultra-fine grained alloys and nanostructured nanocomposites, they have attracted plenty of attention for high technology applications. Severe plastic deformation (SPD) synthesis of these kinds of advanced materials has emerged as a technique with great potential, offering unique microstructural features and mechanical properties stemming from the formation of high-angle nano-grains during processing with uniform dispersion and stability of nanoparticles. In this paper, we present, for the first time, the depth-sensing thermal behavior of ultra-fine grained alloy and nanostructured nanocomposite by conducting interesting hot nano-indentation testing. A newly developed accumulative fold-forging (AFF) process was implemented for imposing the SPD concept and production of ultra-fine grained AA8006 alloy and nanostructured AA8006-B_4C nanocomposite. The present novel work builds on a recent analysis of these materials by describing the nano-scale deformation and softening mechanisms at elevated temperatures using diffusion-based thermal stability models to establish a correlation between nanostructure and mechanical strength under localized nano-scale indenting. Managing the experiments and writing the article was performed by the first author, i.e., Farzad Khodabakhshi. The second author, Adrian P. Gerlich, has founded this research and helped discuss data and proof-reading the manuscript. The nano-indentations measurements were conducted by the third author (Devendra Verma). The fourth author, Martin Nosko, aided with

the EBSD analysis of AFF treated materials. The last author, Meysam Haghshenas, contributed to the discussion of nano-indentation trends and the proof-reading of the manuscript.

Declaration of Competing Interest

The authors declare that they have no known competing financial interests or personal relationships that could have appeared to influence the work reported in this paper.

Acknowledgments

Appendix A. Supplementary data

Supplementary data to this article can be found online at https://doi.org/10.1016/j.matdes.2021.109554.

References

[1] D. Amram, C.A. Schuh, Interplay between thermodynamic and kinetic stabilization mechanisms in nanocrystalline Fe-mg alloys, Acta Mater. 144 (2018) 447–458.

[2] Z. Sun, S. Van Petegem, A. Cervellino, W. Blum, H. Van Swygenhoven, Grain size and alloying effects on dynamic recovery in nanocrystalline metals, Acta Mater. 119 (2016) 104–114.

[3] V. Turlo, T.J. Rupert, Grain boundary complexions and the strength of nanocrystalline metals: dislocation emission and propagation, Acta Mater. 151 (2018) 100–111.

[4] A. Chiba, N. Nomura, Y. Ono, Microstructure and mechanical properties of biomedical co-29Cr-8Mo alloy wire fabricated by a modified melt-spinning process, Acta Mater. 55 (6) (2007) 2119–2128.

[5] P. Ochin, A. Dezellus, P. Plaindoux, J. Pons, P. Vermaut, R. Portier, E. Cesari, Shape memory thin round wires produced by the in rotating water melt-spinning technique, Acta Mater. 54 (7) (2006) 1877–1885.

[6] J. Čížek, M. Janeček, T. Krajňák, J. Stráská, P. Hruška, J. Gubicza, H.S. Kim, Structural characterization of ultrafine-grained interstitial-free steel prepared by severe plastic deformation, Acta Mater. 105 (2016) 258–272.

[7] R.B. Figueiredo, S. Sabbaghianrad, A. Giwa, J.R. Greer, T.G. Langdon, Evidence for exceptional low temperature ductility in polycrystalline magnesium processed by severe plastic deformation, Acta Mater. 122 (2017) 322–331.

[8] Q. Wei, L. Kecskes, T. Jiao, K.T. Hartwig, K.T. Ramesh, E. Ma, Adiabatic shear banding in ultrafine-grained Fe processed by severe plastic deformation, Acta Mater. 52 (7) (2004) 1859–1869.

[9] A. Gholinia, F.J. Humphreys, P.B. Prangnell, Production of ultra-fine grain microstructures in Al-mg alloys by coventional rolling, Acta Mater. 50 (18) (2002) 4461–4476.

[10] S. Gong, M.R. Shankar, Effect of microstructural anisotropy on severe plastic deformation during material removal at micrometer length-scales, Mater. Des. 194 (2020).

[11] T.G. Langdon, Twenty-five years of ultrafine-grained materials: achieving exceptional properties through grain refinement, Acta Mater. 61 (19) (2013) 7035–7059.

[12] C. Ma, S. Suslov, C. Ye, Y. Dong, Improving plasticity of metallic glass by electropulsing-assisted surface severe plastic deformation, Mater. Des. 165 (2019).

[13] A. Vinogradov, V. Patlan, Y. Suzuki, K. Kitagawa, V.I. Kopylov, Structure and properties of ultra-fine grain Cu-Cr-Zr alloy produced by equal-channel angular pressing, Acta Mater. 50 (7) (2002) 1639–1651.

[14] R.Z. Valiev, T.G. Langdon, Principles of equal-channel angular pressing as a processing tool for grain refinement, Prog. Mater. Sci. 51 (7) (2006) 881–981.

[15] Y. Huang, P. Bazarnik, D. Wan, D. Luo, P.H.R. Pereira, M. Lewandowska, J. Yao, B.E. Hayden, T.G. Langdon, The fabrication of graphene-reinforced Al-based nanocomposites using high-pressure torsion, Acta Mater. 164 (2019) 499–511.

[16] T. Müller, M.W. Kapp, A. Bachmaier, P. Felfer, R. Pippan, Ultrahigh-strength low carbon steel obtained from the martensitic state via high pressure torsion, Acta Mater. 166 (2019) 168–177.

[17] F. Kümmel, T. Hausöl, H.W. Höppel, M. Göken, Enhanced fatigue lives in AA1050A/AA5005 laminated metal composites produced by accumulative roll bonding, Acta Mater. 120 (2016) 150–158.

[18] Y. Saito, H. Utsunomiya, N. Tsuji, T. Sakai, Novel ultra-high straining process for bulk materials development of the accumulative roll-bonding (ARB) process, Acta Mater. 47 (2) (1999) 579–583.

[19] K. Peng, Y. Zhang, L.L. Shaw, K.W. Qian, Microstructure dependence of a cu-38Zn alloy on processing conditions of constrained groove pressing, Acta Mater. 57 (18) (2009) 5543–5553.

[20] F. Khodabakhshi, A.P. Gerlich, A. Simchi, A.H. Kokabi, Cryogenic friction-stir processing of ultrafine-grained Al–mg–TiO$_2$ nanocomposites, Mater. Sci. Eng. A 620 (2015) 471–482.

[21] F. Khodabakhshi, A.P. Gerlich, Accumulative fold-forging (AFF) as a novel severe plastic deformation process to fabricate a high strength ultra-fine grained layered aluminum alloy structure, Mater. Charact. 136 (2018) 229–239.

[22] F. Khodabakhshi, A.P. Gerlich, D. Verma, M. Haghshenas, Nano-indentation behavior of layered ultra-fine grained AA8006 aluminum alloy and AA8006-B$_4$C nanostructured nanocomposite produced by accumulative fold forging process, Mater. Sci. Eng. A 744 (2019) 120–136.

[23] F. Khodabakhshi, A.P. Gerlich, M. Worswick, Fabrication and characterization of a high strength ultra-fine grained metal-matrix AA8006-B$_4$C layered nanocomposite by a novel accumulative fold-forging (AFF) process, Mater. Des. 157 (2018) 211–226.

[24] L. Tian, I. Anderson, T. Riedemann, A. Russell, Modeling the electrical resistivity of deformation processed metal-metal composites, Acta Mater. 77 (2014) 151–161.

[25] J. Zhou, R.S. Averback, P. Bellon, Stability and amorphization of cu-Nb interfaces during severe plastic deformation: molecular dynamics simulations of simple shear, Acta Mater. 73 (2014) 116–127.

[26] S.V. Bobylev, I.A. Ovid'Ko, Stress-driven migration of deformation-distorted grain boundaries in nanomaterials, Acta Mater. 88 (2015) 260–270.

[27] S.V. Divinski, G. Reglitz, I.S. Golovin, M. Peterlechner, R. Lapovok, Y. Estrin, G. Wilde, Effect of heat treatment on diffusion, internal friction, microstructure and mechanical properties of ultra-fine-grained nickel severely deformed by equal-channel angular pressing, Acta Mater. 82 (2015) 11–21.

[28] O. Renk, V. Maier-Kiener, I. Issa, J.H. Li, D. Kiener, R. Pippan, Anneal hardening and elevated temperature strain rate sensitivity of nanostructured metals: their relation to intergranular dislocation accommodation, Acta Mater. 165 (2019) 409–419.

[29] L.S. Toth, C.F. Gu, B. Beausir, J.J. Fundenberger, M. Hoffman, Geometrically necessary dislocations favor the Taylor uniform deformation mode in ultra-fine-grained polycrystals, Acta Mater. 117 (2016) 35–42.

[30] M. Kawasaki, I.J. Beyerlein, S.C. Vogel, T.G. Langdon, Characterization of creep properties and creep textures in pure aluminum processed by equal-channel angular pressing, Acta Mater. 56 (10) (2008) 2307–2317.

[31] D.G. Morris, M.A. Muñoz-Morris, High creep strength, dispersion-strengthened iron aluminide prepared by multidirectional high-strain forging, Acta Mater. 58 (18) (2010) 6080–6089.

[32] T. Hayashi, P.M. Sarosi, J.H. Schneibel, M.J. Mills, Creep response and deformation processes in nanocluster-strengthened ferritic steels, Acta Mater. 56 (7) (2008) 1407–1416.

[33] J. Jiang, Y. Zhang, Y. Wang, G. Xiao, Y. Liu, L. Zeng, Microstructure and mechanical properties of thixoforged complex box-type component of 2A12 aluminum alloy, Mater. Des. 193 (2020).

[34] S. Zhu, E. Borodin, A.P. Jivkov, Triple junctions network as the key pattern for characterisation of grain structure evolution in metals, Mater. Des. 198 (2021).

[35] G.M. Pharr, W.C. Oliver, F.R. Brotzen, On the generality of the relationship among contact stiffness, contact area, and elastic modulus during indentation, J. Mater. Res. 7 (3) (2011) 613–617.

[36] O. Engler, G. Laptyeva, N. Wang, Impact of homogenization on microchemistry and recrystallization of the Al-Fe-Mn alloy AA 8006, Mater. Charact. 79 (2013) 60–75.

[37] P. Moldovan, G. Popescu, F. Miculescu, Microscopic study regarding the microstructure evolution of the 8006 alloy in the plastic deformation process, J. Mater. Process. Technol. 153-154 (1–3) (2004) 408–415.

[38] H.G. Jiang, M. Rühle, E.J. Lavernia, On the applicability of the X-ray diffraction line profile analysis in extracting grain size and microstrain in nanocrystalline materials, J. Mater. Res. 14 (2) (1999) 549–559.

[39] Z. Zhang, F. Zhou, E.J. Lavernia, On the analysis of grain size in bulk nanocrystalline materials via X-ray diffraction, Metall. Mater. Trans. A 34 A (6) (2003) 1349–1355.

[40] F. Khodabakhshi, M. Kazeminezhad, The effect of constrained groove pressing on grain size, dislocation density and electrical resistivity of low carbon steel, Mater. Des. 32 (6) (2011) 3280–3286.

[41] F. Khodabakhshi, M. Kazeminezhad, A.H. Kokabi, Constrained groove pressing of low carbon steel: Nano-structure and mechanical properties, Mater. Sci. Eng. A 527 (16–17) (2010) 4043–4049.

[42] B. Völker, V. Maier-Kiener, K. Werbach, T. Müller, S. Pilz, M. Calin, J. Eckert, A. Hohenwarter, Influence of annealing on microstructure and mechanical properties of ultrafine-grained Ti45Nb, Mater. Des. 179 (2019).

[43] W.C. Guo, H. Xu, X.Q. Gao, X.L. Hou, Y. Li, A modified method for hardness determination from Nanoindentation experiments with imperfect indenters, Adv. Mater. Sci. Eng. 2016 (2016) 8.

[44] K. Iwamoto, A. Matsumoto, Franck-Condon factors involving the Morse potential, J. Quant. Spectrosc. Radiat. Transf. 52 (1) (1994) 901–913.

[45] S. Roy, D. Mordehai, Annihilation of edge dislocation loops via climb during nanoindentation, Acta Mater. 127 (2017) 351–358.

[46] H. Somekawa, T. Tsuru, A. Singh, S. Miura, C.A. Schuh, Effect of crystal orientation on incipient plasticity during nanoindentation of magnesium, Acta Mater. 139 (2017) 21–29.

[47] A.J.M. Wood, T.W. Clyne, Measurement and modelling of the nanoindentation response of shape memory alloys, Acta Mater. 54 (20) (2006) 5607–5615.

[48] J.B. Dubois, L. Thilly, P.O. Renault, F. Lecouturier, M. Di Michiel, Thermal stability of nanocomposite metals: In situ observation of anomalous residual stress relaxation during annealing under synchrotron radiation, Acta Mater. 58 (19) (2010) 6504–6512.

[49] M. Abdi, F. Khodabakhshi, A.P. Gerlich, R. Ebrahimi, Characterization of accumulative fold-forged magnesium-nickel multilayered composite structures, Mater. Charact. 167 (2020) 110478.

[50] B. Zhang, Y. Chong, R. Zheng, Y. Bai, R. Gholizadeh, M. Huang, D. Wang, Q. Sun, Y. Wang, N. Tsuji, Enhanced mechanical properties in β-Ti alloy aged from recrystallized ultrafine β grains, Mater. Des. 195 (2020).

[51] F. Khodabakhshi, A. Simchi, The role of microstructural features on the electrical resistivity and mechanical properties of powder metallurgy Al-SiC-Al$_2$O$_3$ nanocomposites, Mater. Des. 130 (2017) 26–36.

[52] F. Khodabakhshi, A. Simchi, A.H. Kokabi, A.P. Gerlich, M. Nosko, Effects of post-annealing on the microstructure and mechanical properties of friction stir processed Al–mg–TiO$_2$ nanocomposites, Mater. Des. 63 (2014) 30–41.

[53] M. Moradpour, F. Khodabakhshi, H. Eskandari, Microstructure–mechanical property relationship in an Al–mg alloy processed by constrained groove pressing-cross route, Mater. Sci. Technol. 34 (8) (2018) 1003–1017.

[54] F. Khodabakhshi, M. Kazeminezhad, The annealing phenomena and thermal stability of severely deformed steel sheet, Mater. Sci. Eng. A 528 (15) (2011) 5212–5218.

[55] F. Khodabakhshi, M. Kazeminezhad, Differential scanning calorimetry study of constrained groove pressed low carbon steel: recovery, recrystallisation and ferrite to austenite phase transformation, Mater. Sci. Technol. (United Kingdom) 30 (7) (2014) 765–773.

[56] F. Khodabakhshi, M. Haghshenas, H. Eskandari, B. Koohbor, Hardness-strength relationships in fine and ultra-fine grained metals processed through constrained groove pressing, Mater. Sci. Eng. A 636 (2015) 331–339.

[57] F. Khodabakhshi, A.P. Gerlich, On the correlation between indentation hardness and tensile strength in friction stir processed materials, Mater. Sci. Eng. A 789 (2020) 139682.